Composite Structures 289 (2022) 115468

Contents lists available at ScienceDirect

Composite Structures

journal homepage: www.elsevier.com/locate/compstruct

Stress state failure analysis of thin-walled GLARE composite members subjected to axial loading in the post-buckling range

D. Banat [a,*], R.J. Mania [a], R. Degenhardt [b]

[a] Department of Strength of Materials, Lodz University of Technology Stefanowskiego 1/15, 90-924 Lodz, Poland
[b] DLR, Institute of Composite Structures and Adaptive Systems, Lilienthalplatz 7, 38108 Braunschweig, Germany

ARTICLE INFO

Keywords:
Thin-walled GLARE
Stress state analysis
Post-buckling
Failure modes
Progressive damage

ABSTRACT

The paper investigated the load-carrying capacity and the participation of stress components in the failure analysis of top-hat-shaped composite columns subjected to uniform compression. GLARE members were axially compressed in laboratory tests employing a static testing unit. Failure tests were monitored in the full load range using the digital image correlation (DIC) system, which enabled visualization of full-field displacements and strains. Simultaneously, FEM numerical simulations were carried out to estimate the load-carrying capacity of the top-hat-shaped sections based on the nominal stress state in both the non-degraded and degraded composite models. In the latter, the material property degradation method (MPDG) allowed a progressive lowering of the material stiffness based on the presumed damage variables. Failure initiation in composite plies was monitored in FE simulations based on Hashin and Puck failure criteria. Stress state analysis was performed to investigate the participation of stress tensor components in the failure function of selected failure criteria. This enabled the identification of critical stresses contributing to aluminum plastic deformation and intra-laminar failure mechanisms that led to the composite fracture. The results of the numerical simulations were found to be in high agreement with the experimental evidence.

1. Introduction

Fiber-reinforced composites have been extensively used in recent years with significant developments in the aerospace, transport, automotive, or construction industries [1,2]. Among all types of composites, modern and new Fiber Metal Laminates (FML) are manufactured by binding metallic layers to fiber-reinforced laminates [3,4]. Herein, some of the composite applications are based on unidirectional glass fiber reinforced prepregs and aluminum alloy sheets (GLARE) [5]. Such a combination of plies guarantees high material strength, enhanced damage, and fatigue tolerances [6]. Different laminate combinations and various fiber alignments or fiber volume ratio can have a significant impact on composite performance. This provides many possibilities for composite manufacturers to design components tailored for specific industrial applications [7,8]. Such structural component solutions have inspired the considerable interest of researchers in recent years in investigating the behavior of composites under specific loading conditions and making recommendations for their advantages and limitations [9–12].

Thin-walled composite structures with open and closed cross-sections are extensively utilized as load-carrying elements, especially in aerospace. The primary function of such structures is to carry axial and bending loads. In the case of axial compression, loss of stability is an unfavorable phenomenon that typically causes a decrease in the strength properties of the structure [13–15]. Nonetheless, it has been demonstrated in various numerical and experimental studies that, after buckling, the structure's ability to carry the compressive load remains stable [16–19]. Regarding comprehensive buckling analysis, separate buckling modes have already been identified for similar thin-walled structures [20–22]. However, there is still considerable uncertainty about their interaction and impact on load-carrying capacity. Hence, many researchers focus on the post-buckling response of composite material structures and the prediction of the structure load-carrying capabilities [13,18,23]. This comprises a failure analysis in order to predict the ultimate strength of multi-layered fiber-reinforced composite columns.

The damage phenomenon must be examined throughout the load range to predict the initiation and propagation of the failure. First, the occurrence of failure in composite material is typically investigated using failure criteria, which consider the state of induced stress and the limits of the material strength to calculate the failure factor [24,25]. As

* Corresponding author.
E-mail address: dominikbanat@gmail.com (D. Banat).

https://doi.org/10.1016/j.compstruct.2022.115468
Received 12 January 2022; Received in revised form 14 February 2022; Accepted 4 March 2022
Available online 9 March 2022

long as isotropic materials are concerned, several failure criteria, including the Huber-Mises-Hencky (HMH) criterion, can be used to successfully determine the material's yield point. Determining an acceptable failure criterion is significantly more challenging for non-isotropic composite materials, whose failure behavior exhibits directional dependency. Many failure studies of anisotropic composites are based on the Hashin criterion, as it was found to provide a satisfactory assessment of fiber and matrix damage separately [14,17,24,26]. Particularly in the case of multi-layered laminates, separate failure criteria are used for different composite constituents to capture the entire failure sequence. Damage evolution is achieved using progressive failure analysis (PFA), in which damage variables control the reduction in stiffness after the start of failure [27]. Thus, appropriate damage initiation and evolution parameters are required to simulate the load-carrying capacity of the structure [18,28].

Various examples of numerical and experimental failure analysis for thin-walled composite columns can be found in other studies [18,29,30]. Based on the literature survey, the most common types of damage in composite structures are intra-laminar failure (matrix cracking and compression or rupture of the tension fiber) and inter-laminar damage (delamination) [31–33]. Fiber degradation has been recognized as the primary factor contributing to the loss of load-carrying capacity of glass fiber-reinforced composites with open cross-sections subjected to uniform compression [32]. On the other hand, delamination growth has been successfully analyzed in FML channel sections using the Cohesive Zone Method (CZM) and the bilinear cohesive contact model [17,18,33]. Preliminary stability and progressive damage analysis of the considered GLARE members were carried out to validate the numerical implementation of the progressive failure algorithm by means of experimental evidence [34]. In this respect, most failure analyses for thin-walled composite columns are devoted to the first-ply failure approach or the continuum damage mechanics (CDM) method [35–37]. Nevertheless, despite significant success in defining the failure phenomenon using the abovementioned methods, there is a lack of physical interpretation of equations of the failure functions and failure induced by specific stresses [25,38–40]. The explanation of damage typically provides only failure factors calculated by quadratic polynomials that are lower than or greater than unity, with no further investigations of the induced stress state and the participation of stress tensor components in material failure. Furthermore, according to the World-Wide Failure Exercise (WWFE), there are no satisfactory theoretical and finite element methods to predict with great precision a failure of multidirectional laminates [41,42]. Failure mechanisms in FMLs were also found to vary with thickness and particular fiber orientation, making it challenging to select suitable methods to capture the entire failure phenomenon [27,43,44]. Hence, in the authors' opinion, there is still insufficient study related to the analysis of multi-failure modes and their propagation in composite materials. Generally, FMLs are characterized by complex failure mechanisms that can occur in metallic and composite plies separately [27,45], which requires further research. Therefore, there is a fundamental need to identify not only failure mechanisms but also their root causes which can be determined utilizing stress state analysis.

In this study, the behavior of thin-walled GLARE members subjected to axial compression was investigated, focusing on post-buckling response and members' load-carrying capacity. This allowed the identification of intra-laminar failure mechanisms, including fibers rupture and matrix cracking or crushing. Herein, the Hashin criterion has been applied for a thorough examination of the composite matrix or the fiber damage initiation phenomenon combined with the stress state analysis performed to assess the critical stresses that lead to failure mechanisms. This required the analysis of stress tensor elements and their contribution to material failure in aluminum and composite plies. Compared with previous work, the originality of this study also includes progressive failure analysis of top-hat-shaped members employing separate fiber and matrix damage variables. These were used to determine the predominant factor and the particular area of the laminate that leads to the propagation of the identified failure mechanisms. The results and discussion presented could provide important information for composite manufacturers that consider failure performance when designing industrial applications of GLARE thin-walled members.

2. Problem statement

The subject of this study is a 7-layered hybrid composite made of alternating layers of the aluminum alloy 2024 T3 (heat-treatable alloy with copper as the primary alloying element) and the unidirectional fiber-reinforced glass–epoxy prepreg TVR 380 M12 26% R-glass (60% fiber volume fraction). The thickness of a single aluminum layer was equal to 0.3 mm, whereas the thickness of a single glass fiber-reinforced prepreg layer after curing was equal to 0.25 mm. The mechanical properties of the aluminum and glass fiber-reinforced prepreg were determined based on experimental tests carried out according to the tensile and three-point bending test standards for fiber-reinforced composites, which were discussed in another study [46,47]. The material response of aluminum plies in the numerical simulation was described by the bilinear isotropic hardening model, which required defining the yield strength ($R_{0.2}$) and the tangent modulus (E_{tang}). The mechanical properties of both constituents of GLARE are presented in Table 1. The multi-method approach and micromechanical analysis to determine the elastic properties of considered composite constituents have been discussed in the comprehensive study by Kamocka et al. [46].

Poisson ratios were determined for the aluminum $\nu = 0.330$ and the composite plies $\nu_{12/13} = 0.269$ and $\nu_{23} = 0.400$, respectively. The numerical study of failure with stress state investigation also required the implementation of the strengths of glass–epoxy unidirectional fiber-reinforced plies according to Table 2. Note that properties of the composite layers were determined for the plane stress state. However, their orthotropic properties were defined for the 3D model according to the specific rules considered for transversely isotropic fiber-reinforced polymers [48].

GLARE specimens were manufactured using the autoclave technique, which allowed the preparation of high-quality multi-layered laminates with high structural homogeneity [49]. Specific manufacturing procedures and curing parameters of the applied autoclave technique were discussed in Ref. [50]. Additionally, the study on the aspects of fiber metal laminate manufacturing also showed that the interface bond between fiber and epoxy has a noticeable impact on transferring stresses throughout the laminate and degradation of this component can decrease the stiffness of the composite [47]. Non-destructive methods of ultrasonic echo testing with the phased array technique were investigated to confirm the absence of defects in the form of porosity or debonding of surfaces throughout the entire volume of laminate [34].

In this study, slender and thin-walled top-hat-shaped sections were investigated. The overall dimensions of the specimens' cross-section are shown in Fig. 1a. Additionally, the radius (R) of the web-flange and flange-lip junctions was ca. 1.75 mm. The geometry of the top-hat-shaped sections was selected based on two main criteria: meeting the requirements of a thin-walled structure and the chosen dimensions had to be found in aircraft components [51]. Laminates consisted of three

Table 1
Mechanical properties of GLARE constituents.

Aluminum [GPa]		GFRP prepreg [GPa]	
E	72	$\mathbf{E_1}$	53.90
G	27.07	$\mathbf{E_2}$	14.92
$\mathbf{R_{0.2}}$	359 * 10^{-3}	$\mathbf{E_3}$	14.92
$\mathbf{E_{tang}}$	720 * 10^{-3}	$\mathbf{G_{12}}$	5.49
		$\mathbf{G_{23}}$	5.33
		$\mathbf{G_{13}}$	5.49

Table 2
Strengths of glass fiber-reinforced layers.

GFRP prepreg	[MPa]
X_t – longitudinal tensile strength	1534
X_c – longitudinal compressive strength	800
Y_t/Z_t – transverse tensile strength	75
Y_c/Z_c – transverse compressive strength	500
$S_{xy} = S_{xz} = S_{yz}$ – shear strength	58

aluminum layers and two embedded plies of composite prepreg (3/2 symmetrical lay-ups). The glass fiber reinforcement in the composite layers was in four different alignments [0//25/45/90] depending on the laminate configuration. This allowed manufacturing various angle-ply laminates: AL/0/90/AL/90/0/AL, AL/90/0/AL/0/90/AL, AL/45/0/AL/0/45/AL, AL/ 0/45/AL/45/0/AL, and AL/0/0/AL/0/0/AL. The selected GLARE lay-up scheme (Al/90/0/Al/0/90/Al) is presented in Fig. 1b. Due to the presence of glass fiber-reinforced prepreg, laminates are considered thin-walled orthotropic plates with transversely isotropic symmetry with respect to the plane perpendicular to the alignment of the fibers.

The previous study by the authors that included a stability and damage analysis of GLARE samples [34,53] has shown that various layouts respond similarly to compressive loading. A satisfactory agreement was achieved between the numerical and experimental methods for all investigated laminate configurations. Therefore, for the purpose of this paper, results are presented for solely selected Al/45/0/Al/0/45/Al and AL/0/0/AL/0/0/AL laminate configurations.

3. Experimental procedures

In laboratory experiments, thin-walled composite specimens were axially compressed using an Instron static testing machine (maximum capacity 200kN) with Zwick/Roel control software. The experimental stand is shown in Fig. 2a. The electromechanical and screw-type strength testing unit enabled displacement control loading with a 1 mm/min crosshead velocity. Laboratory tests were carried out at a room temperature of 23° C. During compressive tests, the GLARE columns were placed in flat bottom grooves milled in plate rigs to limit the lateral displacement of the loaded edges (Fig. 2b). Customized plate rigs mounted on the test stand's upper and lower crossheads guaranteed uniform axial compression of slender and thin-walled GLARE columns. Such a solution of boundary conditions applied during experiments ensured a satisfactory agreement with the simply supported boundary conditions considered in both the numerical and analytical methods [10]. Full-field displacements and strain visualization were measured during experimental trials by the ARAMIS 3D non-contact optical system based on digital image correlation (DIC). The ARAMIS system included a sensor with two digital cameras of 1280 × 1024 px resolution and a maximum total frame rate of 485 images/sec. It allowed three walls to be covered in the tested specimen, that is, the web, the flange, and the lip of the sections shaped like the top hat. The behavior of thin-walled GLARE members was investigated in full load range, focusing on post-buckling response. Results of experimental load-shortening curves are presented in the previous study [34].

4. Numerical computations

The model of a 7-layer GLARE sample was prepared in the Finite Element Method (FEM) using the structural element type SHELL181 available in the commercial software package ANSYS®. According to the ANSYS documentation [54], a selected four-node element type with six degrees of freedom at each node is typically used in multi-layered applications of thin-walled composites or sandwich structures. The implementation of shell element type with section parameters enabled independently defining individual layers of the laminate (material properties, layer's thickness, direction of the principal axes of the orthotropic material). Herein, layers of glass–epoxy fiber-reinforced prepreg were modeled by linear-elastic material properties and strengths obtained in experimental tests. The elastic–plastic material response of the aluminum plies in the numerical simulation was described by the bilinear isotropic hardening model. The material parameters of the composite constituents and the strengths of the transversely isotropic glass fiber-reinforced plies are shown in Table 1 and Table 2, respectively. This numerical model was prepared to perform failure analysis of individual laminate constituents. This allowed investigating the modes of initiation of aluminum plastic deformation and intra-laminar damage in composite plies. The contact between alternating laminate layers was not modeled.

In the FE model, it was assumed that the column is subjected to uniform axial compression to ensure boundary conditions consistent with experimental tests [10]. Therefore, simply supported displacements were limited at both ends of the column and the load was implemented in the form of a concentrated compressive force. Additionally, coupling constraints (constant value of the displacement along

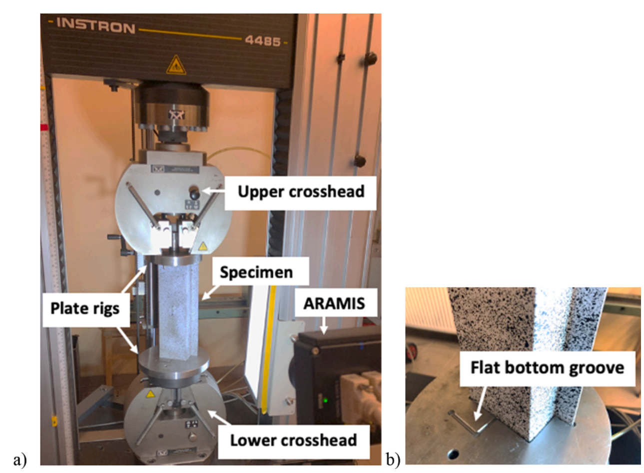

Fig. 2. Experimental stand of Instron static testing machine (a) and flat bottom grove in plate rig (b).

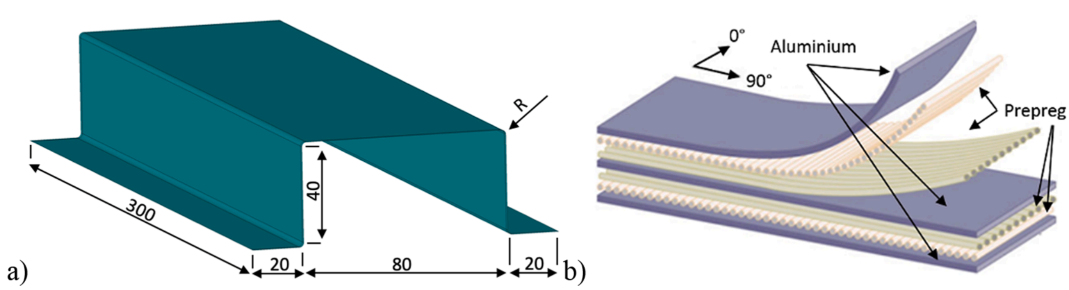

Fig. 1. Dimensions of top-hat-shaped section (a) and sample laminate lay-up (b) [52].

the load axis) were introduced along loaded edges to fulfill the condition of rectilinear column edges and displace uniformly along the column length (uniform shortening of the column). Mesh refinement was implemented to model flat bottom grooves through displacement constraints in the direction perpendicular to the surface of a column's walls at a distance of 2 mm from the columns' ends. This corresponded to experimental procedures, wherein flat bottom grooves were milled in plate rigs to limit the lateral displacement of loaded edges (as presented in Fig. 2b). Mesh refinement was also achieved using a cylindrical coordinate system applied locally at circular corners between the web-flange and flange-lip arc connections of the top-hat-shaped section. The mesh size and mesh convergence analysis were further discussed in another study [34].

The linear buckling analysis (LBA) was performed to establish the critical buckling load and the appropriate buckling mode shapes. Subsequently, a geometrically non-linear analysis was carried out to find a solution in the post-buckling range. Herein, the load factor was normalized in the non-linear analysis concerning the first buckling load obtained in the LBA. Considered slender and thin-walled open-cross sections are also sensitive to wall imperfections affecting members' post-buckling response. Hence, the first local buckling mode shape obtained in the linear analysis was also projected onto the nodal mesh of the finite element model to ensure walls imperfections. Initial imperfections were referred to 0.01 of the members' wall thickness. Solution for nonlinear buckling problem was determined by incremental Newton-Raphson procedure, wherein arc-length method was applied to avoid convergence issues. The geometrically non-linear analysis was used to study columns post-buckling response and predict the load-carrying capacity.

4.1. Load-carrying capacity (LCC) prediction

A numerical model of top-hat-shaped GLARE specimens was initially used in the geometrically non-linear analysis to determine the column's load-carrying capacity (LCC). First, the equilibrium equations in the non-linear analysis were solved using the Newton-Raphson algorithm, in which the stiffness matrix was updated with each iteration of incremental load. Herein, equilibrium paths were determined based on the nominal stress state of a non-degraded structure. Second, the material property degradation method (MPDG) was used to introduce the linear damage evolution law. Based on the damage variables (d_f, $d_{m,}$) the stiffness was gradually reduced in the finite element where the failure process was initiated. Failure initiation was monitored by failure factors greater than one (FF > 1), determined by the Hashin failure criterion. Hence, once the Hashin criterion identified the initiation of failure, damage variables were used to degrade the tensor of mechanical properties. The material property degradation approach was used following guidelines given in Refs. [37,55,56]. Nevertheless, MPDG was used solely to simulate stiffness degradation in composite layers. Hence, the post-buckling response of aluminum layers was investigated separately in a non-degraded structure using the Huber-Mises-Hencky criterion. In this respect, the numerical computation of LCC was performed for two separate numerical models:.

- Geometrically non-linear analysis with the nominal stress state of a non-degraded structure (FEM_non_degraded). The load-carrying capacity was analyzed in aluminum plies based on the equivalent stresses determined by the Huber-Mises-Hencky criterion. Equivalent stresses were further compared to the material yield strength limit.
- Progressive failure analysis with the reduction in composite stiffness after the initiation of failure. The load-carrying capacity was analyzed in composite plies based on maximum load from post-buckling equilibrium paths.

Additionally, failure criteria were used throughout non-linear analysis with incremental load to monitor the change of failure factors in each load step. This considered the calculation of failure factors for the Hashin fiber (HFIB) and Huber-Mises-Hencky (HMH) criterion. For the latter, the failure factor (HMH FF) was determined as the ratio of equivalent stresses (σ_{EQV}) and yield strength limit ($R_{0.2} = 359$ MPa) as given in Eq. (1). It presumed that the load-carrying capacity prediction was based on the Huber-Mises-Hencky criterion at the point where the equivalent stresses exceed the aluminum yield limit.

$$HMHFF = \frac{\sigma_{EQV}}{R_{0.2}} \tag{1}$$

The increase of failure factors for incremental load substeps in aluminum and composite plies was investigated to observe which laminate constituents govern the laminate response in compressive failure tests.

4.2. Participation of stress components in the failure and progressive damage

Subsequently, stress state analysis was performed for top-hat-shaped composite columns subjected to uniform axial compression. This enabled investigating the participation of stress tensor components in the failure function of selected Huber-Mises-Hencky and Hashin failure criteria analyzed in separate laminate plies. For this reason, the nodal data were sorted to select the highest value of the equivalent stress (σ_{EQV}) or failure factor determined by the abovementioned criteria in aluminum and composite plies, respectively. For the chosen node location, the stress tensor elements that corresponded to the coordinate system x, y, z were recorded in a data file.

For layers of isotropic aluminum material, the equivalent stress (σ_{EQV}) was determined according to Eq. (2).

$$\sigma_{EQV} = \left(\frac{1}{2}\left[\left(\sigma_x - \sigma_y\right)^2 + \left(\sigma_y - \sigma_z\right)^2 + \left(\sigma_z - \sigma_x\right)^2 + 6\left(\sigma_{xy}^2 + \sigma_{yz}^2 + \sigma_{xz}^2\right)\right]\right)^{\frac{1}{2}} \tag{2}$$

In composite layers, the Hashin criterion was used to calculate failure factors separately for matrix (HMAT) and fiber (HFIB) damage. For the analysis of the stress state, analytical formulas were also applied for the HMAT and HFIB failure factors (as given in Eqs. (3) and (4)) according to Ref. [57]. Stress analysis based on the Hashin failure criterion was performed to obtain in-plane stress components. The allowable stress limits for the transversely isotropic material were introduced according to the strength characteristics collected in Table 2.

$$f_f = \begin{cases} \left(\frac{\sigma_x}{X_t}\right)^2 + \frac{{\sigma_{xy}}^2 + {\sigma_{xz}}^2}{{S_{xy}}^2} if \sigma_x > 0 \\ \left(\frac{\sigma_x}{X_c}\right)^2 if \sigma_x < 0 \end{cases} \tag{3}$$

$$f_m = \begin{cases} \left(\frac{\sigma_y + \sigma_z}{Y_t}\right)^2 + \frac{{\sigma_{yz}}^2 - \sigma_y\sigma_z}{{S_{yz}}^2} + \frac{{\sigma_{xy}}^2 + {\sigma_{xz}}^2}{{S_{xy}}^2} if \sigma_y + \sigma_z > 0 \\ \frac{1}{Y_c}\left[\left(\frac{Y_c}{2S_{yz}}\right)^2 - 1\right]\left(\sigma_y + \sigma_z\right) + \left(\frac{\sigma_y + \sigma_z}{2S_{yz}}\right)^2 + \frac{\sigma_{yz}^2 - \sigma_y\sigma_z}{S_{yz}^2} + \frac{\sigma_{xy}^2 + \sigma_{xz}^2}{S_{xy}^2} if \sigma_y + \sigma_z < 0 \end{cases} \tag{4}$$

The stress state analysis allowed for the identification of critical stresses that led to aluminum plastic deformation and the initiation of intralaminar failure mechanisms in composite plies. A further study included progressive failure analysis using the degradation method of material properties. Separate fiber and matrix damage variables were used to introduce the damage evolution law. This allowed us to predict separate damage modes for fiber tensile, fiber compressive, and matrix tensile, matrix compressive, interlayer shear damage variables. The numerical results were compared with the experimentally damaged specimen. Constitutive laws of progressive damage modeling including softening law have been discussed in another study dedicated to progressive failure of thin-walled Z-shaped FML members subjected to axial compression [58] or GFRP pipes subjected to transverse loading [59]. Numerical progressive failure analysis can also be performed utilizing continuum damage mechanics (CDM), for which a layer where the failure occurred is replaced by a virtual continuum ply with reduced mechanical properties. The linear damage evolution law combined with a linear material softening law is used to decrease the stiffness of the failed ply [60]. CDM approach can be combined with failure criteria and fracture mechanics for predicting damage initiation and propagation by coupling the internal state variables [61]. It enables the control of the energy dissipation required for the evolution of the separate damaged states. In this sense, failure modes such as fiber rupture, longitudinal and transverse matrix cracking are associated with respective fracture energies and material properties are progressively degraded until complete failure of composite constituents [62]. Therein, damage variables are defined in order to quantify damage concentration associated with failure modes and predict the gradual stiffness reduction during the damage process [63]. However, the energy-based stiffness degradation method according to CDM theory, requires the definition of damage variables based on the energies dissipated per unit area and the viscous damping parameters [54], which were not considered in this study. CDM modeling will be performed in a further research that will include the numerical implementation of softening constitutive equations [64]. This would also require defining damage variables based on energy release rates, which could be determined experimentally [59,61]. In this respect, the continuum damage model will enable a full characteristic of the composite failure mechanisms. However, the authors emphasize that energy dissipation is also related to the size of finite elements, resulting in mesh-dependent results.

5. Results and discussion

5.1. Analysis of load-carrying capacity

The load-carrying capacity (LCC) of top-hat-shaped GLARE columns was determined numerically based on geometrically non-linear analysis and experimentally based on ARAMIS 3D non-contact system with digital image correlation (DIC) method. Initially, the value of LCC was forecasted based on the Huber-Mises-Hencky criterion applied to the FEM model with non-degraded material structure (denoted as FEM_non_degraded_HMH). Subsequently, LCC was determined using post-buckling equilibrium paths for the FEM model with a degraded composite structure (denoted as FEM_degraded). Herein, the reduction in material stiffness was controlled using different values of damage variables that were determined separately for the fiber (d_f) and matrix (d_m) in the range from 0.5 to 1. Damage variables with values lower than 0.5 were not considered in FEM since they were found in another study to be less in agreement with experimental tests [32]. As a result, numerical analysis was carried out for the following (FEM_degraded) models:.

- FEM_degraded_1:$d_f = 0.5$, $d_m = 0.5$
- FEM_degraded_2:$d_f = 0.5$, $d_m = 0.75$
- FEM_degraded_3:$d_f = 0.75$, $d_m = 0.75$
- FEM_degraded_4:$d_f = 1$, $d_m = 1$

The results of LCC that include experimental (EXP) and numerical methods (FEM) are gathered in Table 3. The relative difference as the LCC value (given as a percentage) was calculated to assess the consistency between various methods. Comparison of numerical and experimental load–displacement curves and mapping failure criteria onto the deformation contour of considered top-hat-shaped sections is presented in the authors' prior study [53]. This also included numerical computation of equivalent stresses (EQVS) for aluminum layers that were projected onto the profile geometry. In laboratory tests, the surface deformations were measured by ARAMIS 3D optical system, which

Table 3
Load-carrying capacity comparison based on FEM models and experiments.

Sample	Method		Load-Carrying Capacity - LCC [kN]	EXP vs. FEM [%] (Relative difference)
Al/45/0/Al/0/45/Al	Experimental test – ARAMIS (EXP)		78.55	N/A
	Numerical	FEM_degraded_1	82.17	4.40
	Numerical	FEM_degraded_2	80.61	2.55
	Numerical	FEM_degraded_3	79.62	1.34
	Numerical	FEM_degraded_4	79.44	1.12
	Numerical	FEM_non_degraded_HMH	78.91	0.45
Al/0/0/Al/0/0/Al	Experimental test -ARAMIS (EXP)		83.88	N/A
	Numerical	FEM_degraded_1	88.65	5.38
	Numerical	FEM_degraded_2	88.52	5.24
	Numerical	FEM_degraded_3	88.50	5.22
	Numerical	FEM_degraded_4	88.34	5.05
	Numerical	FEM_non_degraded_HMH	85.71	2.14

allowed to monitor the specimen's failure behavior in full load range until fracture. Presented results were found to be in good agreement with an experimentally damaged specimen. Furthermore, FEM and experimental post-buckling equilibrium paths (load-shortening curves) were investigated in the previous study by the authors [34]. Since the results provided satisfactory agreement, solely load-carrying capacity prediction is shown in the current study of top-hat-shaped GLARE columns subjected to uniform compression. Additionally, damage modes' contours of progressive failure analysis are shown in Fig. 5.

The percentage difference between experiments and FEM models with degraded material structure (FEM_degraded) ranges from 1.12% to 4.40% for the Al/45/0/Al/0/45/Al sample and from 5.05% to 5.38% for the Al/0/0/Al/0/0/Al sample, respectively. For both laminate configurations, the highest consistency of the EXP vs. FEM comparison was achieved for the FEM_degraded_4 model ($d_{f/m} = 1$). Damage variables equal to unity indicate a reduction in composite stiffness throughout after damage initiation in specified finite elements. Comparative analysis of various numerical models has shown that using high values of material damage variables in MPDG allows for the greatest correlation between experimental and numerical methods. Similar results were presented in the progressive failure analysis of slender 8-layered GFRP composite structures subjected to compression [32], wherein the stiffness degradation parameters ($d_{f/m} \geq 0.9$) provided satisfactory agreement between numerical and experimental methods. These can suggest a recommendation for selecting damage variables in the failure analysis of thin-walled components under axial compression. Nevertheless, different loading scenarios should also be investigated in a similar way and validated by experimental tests to minimize the potential discrepancy in the results achieved.

Furthermore, according to the findings of a progressive damage analysis performed for comparable Z-shaped sections of fiber metal laminates [58], $d_{f/m}$ variables should take into account varying susceptibility to damage of two composite constituents. Hence, in the FEM_degraded_2 model, different values of damage variables were used for fiber ($d_f = 0.5$) and matrix ($d_m = 0.75$), respectively. However, based on the results gathered in Table 3, it has been concluded that the damage variables in the range of $< 0.5{,}1 >$ considered in progressive failure models (FEM_degraded) have only a limited impact on the load-carrying capacity of columns. This further indicates that the post-critical response of considered GLARE members is governed by aluminum material, and damage evolution law applied to composite layers did not substantially affect the load-carrying capabilities of the entire laminate.

The results of the load-carrying capacity also showed that the lowest relative difference between the experiment and the FEM methods was obtained for the FEM_non_degraded_HMH model (Table 3). In such a model, the equivalent stresses (σ_{EQV}) were calculated within aluminum sheets and further compared to the material yield strength limit (R_{02} =

359 MPA). The percentage difference between the numerical and experimental methods was equal to 0.45% and 2.14% for the Al/45/0/Al/0/45/Al and Al/0/0/Al/0/0/Al laminates, respectively. The high consistency of LCC prediction achieved for the FEM_non_degraded_HMH method suggests that aluminum plies control the post-critical behavior of 7-layered thin-walled GLARE columns under consideration. In this respect, the Huber-Mises-Hencky criterion applied in aluminum layers can be used with a reasonable degree of success to predict the loss of load-carrying capacity of GLARE members.

Susceptibility to failure of laminate constituents was also analyzed by introducing failure criteria throughout the entire non-linear analysis with incremental load increase. For that purpose, the Huber-Mises-Hencky (HMH) criterion was applied to determine the equivalent stresses in aluminum plies. Subsequently, Huber-Mises-Hencky failure factors (denoted as HMH FF) were calculated on the basis of equivalent stresses and the yield strength limit as proposed in Eq. (1). The Hashin fiber failure criterion was used to calculate failure factors (for comparison, denoted as HFIB FF) in composite plies. In this analysis, failure factors were determined based on the nominal stress state in the non-degraded model of GLARE constituents. Results of FF calculated for incremental load rise for selected laminate configuration (Al/0/0/Al/0/0/Al) are shown in Fig. 3.

The results of failure criteria introduced throughout the nonlinear analysis with incremental load showed that the loss of load-carrying capacity is first predicted by the Huber-Mises-Hencky criterion applied to aluminum plies. This corresponds to the load 85.71kN, for which the failure factor (HMH FF) reached a value of 1. One can also notice a sharp growth of Hashin fiber failure factor (HFIB FF) at the point where equivalent stresses in the aluminum layers reached the yield limit (HMH FF > 1). This also confirms that the entire response of 7-layered GLARE columns is governed by aluminum layers, and the Huber-Mises-Hencky criterion can be successfully used to determine the loss of load-carrying capacity. Furthermore, the slope of the plot curve changes significantly at the load corresponding to the critical force (approx. 62kN) of the top-hat-shaped GLARE sections. According to another study carried out for similar fiber metal laminates subjected to axial compressive loading, the bilinear isotropic model applied to aluminum plies was found to affect significantly local buckling phenomena [10].

5.2. Stress state analysis

Another analysis was performed to investigate the participation of stress tensor components in the failure functions of the Huber-Mises-Hencky (Eq. (1) and Eq. (2)) and Hashin criteria (Eq. (3) and Eq. (4)) in aluminum and composite layers, respectively. The main purpose of defining contribution of each stress component was the identification of

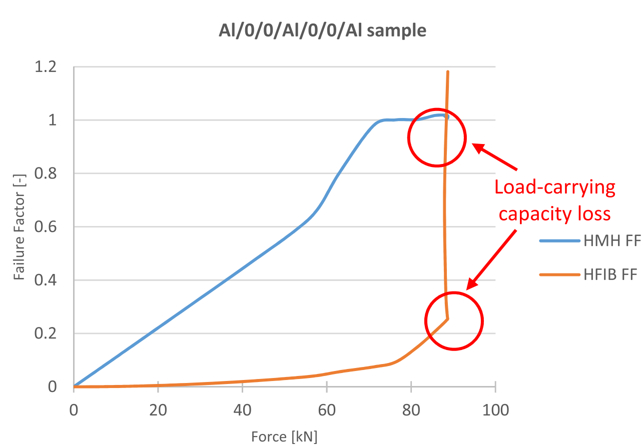

Fig. 3. Failure factors determined by Huber-Mises-Hencky and Hashin criteria for incremental load rise.

critical stresses contributing to aluminum plastic deformation and intra-laminar failure mechanisms that led to the composite damage. Initially, stress tensor elements were collected for the nodal location that reached the highest equivalent stress (σ_{EQV}) calculated in aluminum layers, i.e., outer layers (L1 and L7) and the inner layer (L4). The results are collected in Table 4. Note that the middle position of the layer was selected. It has been recognized that in considered laminate analysis, stress and strains do not change rapidly across defined lamina thickness [65]. Furthermore, based on a comparative study on relations between various layers of top-middle-bottom, compliance of failure factors was obtained with minor mutual differences resulting from the plate bending model and the layer symmetry of the configuration of the layers [66]. The normal stress component σ_z was presumed to be equal to zero in accordance with the classical laminate plate theory. After that, the participation of stress tensor elements in Huber-Mises-Hencky failure factors was determined and presented in Table 5.

Splitting the failure function into four parts suggests that the stress component σ_x had a dominant contribution towards Huber-Mises-Hencky equivalent stresses and consequently had a significant impact on the failure factor (HMH FF). In each layer considered, the Huber-Mises-Hencky failure factor is greater than unity (HMH FF > 1), indicating that the equivalent stresses exceed the aluminum yield limit. In this respect, compressive stress (σ_x) contributes to the greatest extent to the aluminum failure, which takes the form of plastic deformation.

Further analysis was carried out to establish the stress tensor elements in the composite layers in the area where the Hashin criterion reached the highest value, which implies the potential occurrence of material damage. Separate failure factors were determined for the Hashin fiber failure criteria (HFIB) and matrix (HMAT) under load equal to column load-carrying capacity. The stress state is presented for randomly selected layers L3 and L5 (see Table 6). Additionally, stress distribution for each composite layer (L2, L3, L5, L7) is shown in Fig. 4. Stress distribution was determined in nodal data where the Hashin matrix failure criterion (HMAT) indicates failure initiation (HMAT FF > 1). Hashin failure criterion is used to identify the initiation of intra-laminar damage in composite layers. Different damage initiation mechanisms are evaluated to account for fiber tension, fiber compression, matrix tension, matrix compression and in-plane shear failure modes, respectively [57,59]. Based on the Rafiee and Torabi work that investigated stress analysis based on multiple failure criteria [57], Hashin criterion estimated the composite failure with higher levels of accuracy when compared to experimental data.

A similar stress distribution is observed in each composite layer, which results from the symmetry of the lay-ups configuration in 7-layered GLARE specimens. Note that nominal stress values are presented in Fig. 4 (values were not scaled and not changed to absolute values), which shows that due to the interlaminar force, shear stress σ_{xy} has a positive value in layers L2 and L3 and a negative value in layers L5 and L6. It confirms that symmetry is preserved with respect to laminate middle layer L4. This also indicates that boundary conditions in FEM are in agreement with experimental tests, wherein customized plate rigs mounted on the test stand's upper and lower crossheads enabled uniform axial compression. Furthermore, the participation of stress tensor elements within Hashin failure factors was determined and the results are presented in Table 7 and Table 8. Analytical formulas for Hashin fiber (f_f) and matrix (f_m) failure criteria were shown in Eq. (3) and Eq. (4), respectively. In this approach, the failure functions were also divided into parts to assess the critical stresses that cause damage to the composite.

Substituting composite strengths and particular stress tensor components into the Hashin failure criteria functions allowed assessing the share of the particular part in material failure. Herein, Hashin criteria in FE computations consider various failure mechanisms by developing four different intra-laminar damage initiation modes: fiber tension (rupture/breakage), fiber compression (kinkling), matrix tension

Table 4
Stress tensor components in aluminum layers.

Layer	Criteria	σ_{EQV} [MPa]	FF [-]	σ_x [MPa]	σ_y [MPa]	σ_{xy} [MPa]	σ_{yz} [MPa]	σ_{xz} [MPa]
L1	HMH	363.68	**1.01**	−336.39	−16.20	−88.91	−1.41	−13.91
L4	HMH	383.60	**1.07**	−350.55	−45.74	−64.56	−92.53	2.16
L7	HMH	364.96	**1.02**	−359.02	−36.53	72.57	1.17	−9.68

Table 5
Participation of stress tensor components in the Huber-Mises-Hencky failure factor.

Layer	$\frac{1}{2}(\sigma_x-\sigma_y)^2$	$\frac{1}{2}(\sigma_y-\sigma_z)^2$	$\frac{1}{2}(\sigma_z-\sigma_x)^2$	$\frac{1}{2}\left(6\left(\sigma_{xy}^2+\sigma_{yz}^2+\sigma_{xz}^2\right)\right)$	σ_{EQV}= SQRT(SUM)	HMH FF= $\frac{\sigma_{EQV}}{R_{0.2}}$
L1	51258.58	131.25	56577.43	24298.98	363.68	**1.01**
L4	46454.57	1046.21	61443.70	38200.93	383.60	**1.07**
L7	51999.90	667.18	64447.32	16084.36	364.96	**1.02**

Table 6
Stress tensor components in composite layers.

Layer	Criteria	FF [-]	σ_x [MPa]	σ_y [MPa]	σ_{xy} [MPa]	σ_{yz} [MPa]	σ_{xz} [MPa]
L3	HFIB	**1.01**	8.02	−69.04	58.16	−11.39	−5.36
L5	HFIB	**1.17**	9.80	−86.83	62.17	−2.42	−7.70
L3	HMAT	**1.12**	−146.06	−24.66	8.39	24.76	−1.04
L5	HMAT	**1.01**	−142.56	−23.08	−10.09	20.79	−2.23

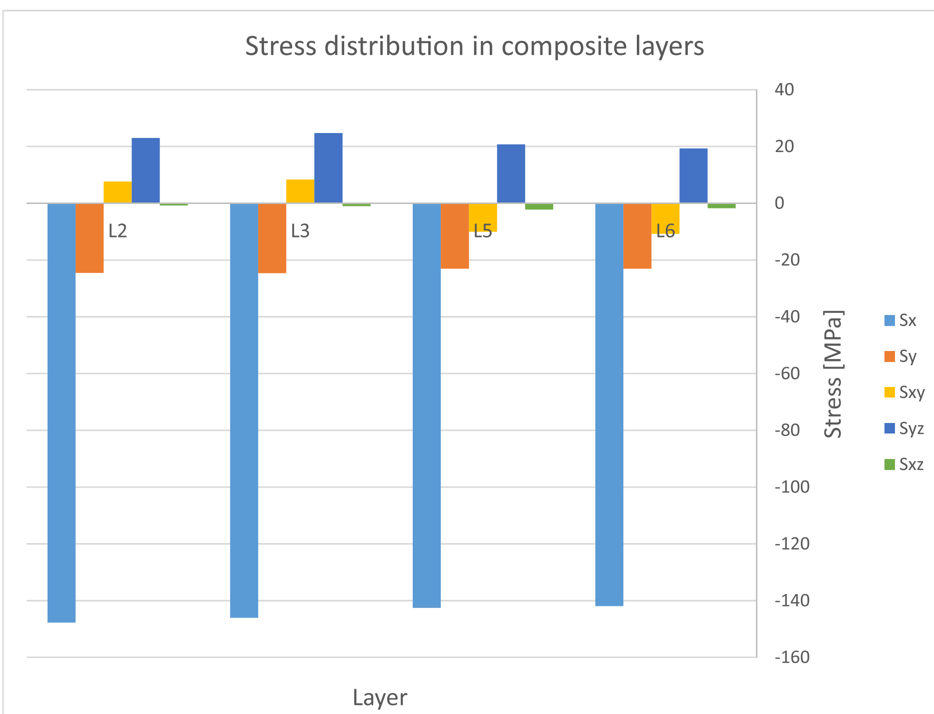

Fig. 4. Stress distribution for each composite layer in nodal data determined by Hashin matrix failure criterion (HMAT FF > 1).

(cracking), and matrix compression (crushing) [24,54].

Hence, the implementation of the Hashin criterion in the numerical study allows predicting the first failure occurrence, and further stress state analysis enables the identification of the damage initiation mode. Analysis of the stress tensor components (Table 7) showed that the part of the Hashin fiber failure function that includes the interaction of shear stresses has the most significant impact on the failure factor (f_f). Hence, the characteristics of the Hashin damage initiation modes indicate that fiber rupture ($\sigma_x > 0$) is caused predominantly by shear stresses (σ_{xy} and σ_{xz}) and their interaction with composite' shear strength (S_{xy}). This is in agreement with a comparative study of the Hashin damage criterion applied to composite failure [24], which found that fiber rupture occurs at the point of maximum shear stressσ_{xy}. Low values of Hashin fiber failure function component that includes normal stress σ_x (Table 7) also confirm high strength of glass–epoxy unidirectional fiber-reinforced plies in an axial direction parallel to fibers. On the other hand, matrix

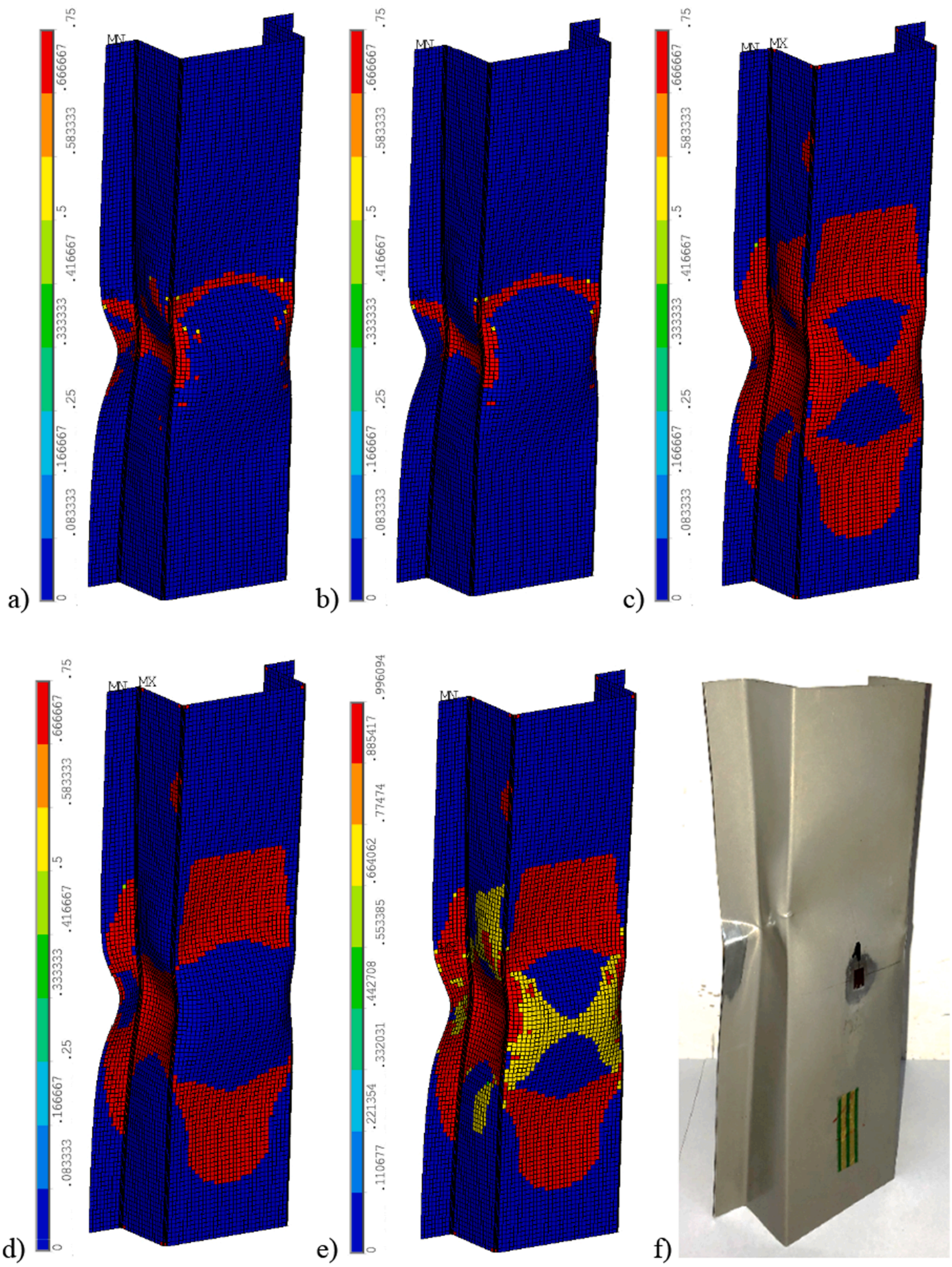

Fig. 5. Damage modes of a) fiber tensile, b) fiber compressive, c) matrix tensile, d) matrix compressive, e) interlayer shear damage variables compared with the experimentally damaged specimen (f).

Table 7
Participation of stress tensor components in the Hashin fiber failure criterion.

Layer	$\left(\frac{\sigma_x}{X_t}\right)^2$	$\frac{\sigma_{xy}{}^2+\sigma_{xz}{}^2}{S_{xy}{}^2}$	HFIB (f_f) = SUM
L3	0.00	1.01	**1.01**
L5	0.00	1.17	**1.17**

crushing ($\sigma_y < 0$) within GLARE members is caused predominantly by compressive stress σ_y and shear stress σ_{yz} components. Furthermore, the transverse compressive strength (Y_c) and shear strength (S_{yz}) defined for transversely isotropic composite plies have the most significant impact on the Hashin matrix failure factor (f_m). Such results for symmetrical laminate configuration and longitudinal fiber alignment indicate that the shear stress state contributes primarily to the matrix failure, which is also in agreement with other studies [35]. Nevertheless, it has been recognized that, for compressive loading, the damage of the matrix did not have a significant impact on the ultimate strength of multi-layered fiber-reinforced composite columns [32]. Therein, progressive failure analysis indicated that loss of load-carrying capacity is mainly affected by fiber degradation, which leads to a significant decrease in the stiffness of the entire material.

Table 8
Participation of stress tensor components in the Hashin matrix failure criterion.

Layer	$\frac{1}{Y_c}\left[\left(\frac{Y_c}{2S_{yz}}\right)^2-1\right](\sigma_y+\sigma_z)$	$\left(\frac{\sigma_y+\sigma_z}{2S_{yz}}\right)^2$	$\frac{\sigma_{yz}^2-\sigma_y\sigma_z}{S_{yz}^2}$	$\frac{\sigma_{xy}^2+\sigma_{xz}^2}{S_{xy}^2}$	HMAT (f_m) = SUM
L3	0.87	0.05	0.18	0.02	**1.12**
L5	0.81	0.04	0.13	0.03	**1.01**

5.3. Progressive damage modes

Stress state analysis and the identification of critical stresses that led to composite failure were performed to forecast the first occurrence of failure in selected composite layers. Nevertheless, the damage of composite material tends to develop gradually throughout the laminate after the onset of the failure. Therefore, an attempt has also been made to assess the damage variables of considered top-hat-shaped GLARE members and predict progressive damage modes of matrix and fiber failure separately. This includes fiber tensile damage variable (FT), fiber compressive damage variable (FC), matrix tensile damage variable (MT), matrix compressive damage variable (MC), and interlayer shear damage variable (S). The results of damage maps for the selected progressive model PFA_3 ($d_{f/m}$ = 0.75) are shown in Fig. 5. Herein, FF = 0.75 indicates complete damage for FT, FC, MT, MC variables. For the shear damage variable (S), the maximum failure factor (FF = 0.996) was calculated based on the stiffness reduction coefficients [55]. FE computations were carried out for the load substep that corresponded to the load-carrying capacity of the member.

For each damage variable, failure was initiated at the midlength of the web-flange joint and propagated towards the web and the flange of the member. Material damage of top-hat-shaped sections also occurred along the midlength of lip-free edges, which are extensively exposed to the bending phenomenon in the post-buckling state. The results of the progressive damage modes showed that the highest concentration of matrix tensile damage variable (MT = 0.75) was induced at the midlength of the column (Fig. 5c). This could result from the relatively low transverse tensile strength of the composite plies (Y_t = 75 MPA) compared to its compressive strength (Y_c = 500 MPA). Based on the abovementioned stress state analysis, the first failure occurrence of the matrix took the form of crushing. Thereafter, progressive damage analysis was crucial to forecast the further propagation of matrix failure, which is mainly affected by cracking. This is also in agreement with other studies that have recognized that the most common form of intra-laminar failure in composite structures is matrix cracking and fiber rupture [31,32]. The onset of matrix cracking is expected at the point of the maximum tensile stress [24]. Similar results were achieved in the PFA study of C-shaped profiles subjected to uniform compression [32]. The failure of the top-hat-shaped members was also highly affected by the interlayer shear damage variable (Fig. 5e). According to the literature [18], fulfilling the damage evolution law that concerns damage of the composite material due to matrix tension and shear (Fig. 5c and Fig. 5e), there is a high possibility of the delamination phenomenon. Based on research by Lin et al. on FML damage, fiber rupture contributes to the delamination between FRP and aluminum plies, whereas matrix cracking affects debonding within embedded FRP layers [27]. In this regard, failure in GLARE members occurring on the boundary surface of the layer can also provide inter-laminar delamination. Nevertheless, inter-laminar delamination is not considered in this study. The analysis of delamination requires an analysis of contact interface stresses and the growth of delamination using the cohesive contact model [59], which was not the subject of the current research. The cohesive zone is established by a constitutive law determining a correlation between the traction vector and the resultant interfacial separation. In a surface-based cohesive zone, the adhesion between adjacent layers is defined as an interaction through a zero-thickness interface. On the other hand, the cohesive contact element method is also used to model the adhesion between layers as the material with specific mechanical properties and thickness [59]. The delamination growth of GLARE channel sections using the Cohesive Zone Method (CZM) and the bilinear cohesive contact model has been thoroughly assessed in another study [33]. It investigated numerically the initiation and propagation of the layer debonding within the 7-layered GLARE samples, which was validated by an experimental test. In Kamocka's study, the inter-laminar delamination was tracked by interlaminar stresses and gap distance. Numerical calculations revealed the initiation of delamination failure in the members' free edges and its propagation along these edges. This is in agreement with the current study of intra-laminar failure mechanisms, wherein damage of top-hat-shaped sections also occurred along the midlength of lip-free edges, which are extensively subjected to the bending phenomenon in the post-buckling state. Another researcher also investigated the delamination buckling of GLARE members subjected to a compressive force, which included solid-shell element type to model individual layers [67]. It required modeling interface elements that were capable of capturing the delamination phenomenon. Hence, an attempt has already been made to predict successfully the inter-laminar delamination phenomenon in considered fiber-metal laminates. In this respect, the current study focuses predominantly on identifying critical stresses contributing to intra-laminar failure mechanisms (including fibers rupture and matrix cracking or crushing) that led to the composite damage.

The FE solution for the progressive damage model is consistent with the stress state analysis mentioned above, wherein the matrix and fiber damage initiation modes were predominantly caused by shear stresses. This is in comparison to the agreement with the comparison of multiple failure criteria performed for FML Z-shaped specimens subjected to uniform compression [66]. Therein, according to the Hashin criterion, shear stresses contribute greatly to the composite failure. This also confirms that unidirectionally reinforced composites can be tailored to carry high axial loads in the direction parallel to fibers.

Furthermore, due to the symmetry of the top-hat-shaped geometry, similar damage modes were noticed on both sides of the GLARE specimen. The results of the FEM analysis were consistent for each laminate configuration and were found to be in good agreement with the experimentally damaged samples (Fig. 5f). This compliance between numerical and experimental evidence also proved that the design of the boundary conditions in the FE model was in good agreement with the experimental plate rigs that ensured axial compression during laboratory failure tests. Note that damages in experimentally compressed specimens were analyzed post-experiment. Therefore, it was challenging to observe the type of failure initiation and propagation during the loading process. For that reason, further research might require the application of a high-speed camera or the analysis of the damaged material structure using digital microscopes. This would allow for the precise registration of the failure phase and the complete characteristics of the failure propagation in the laminate.

6. Conclusions

This paper studies the load-carrying capacity and the participation of stress components in the failure of multi-layered GLARE members subjected to axial compressive loading. The behavior of thin-walled top-hat-shaped members was investigated with a primary focus on the post-buckling response.

Research presented in this paper lead to several key findings:.

- The load-carrying capacity of top-hat-shaped GLARE sections determined numerically by the geometrically non-linear analysis was consistent with experimental measurements. The relative difference between FEM and the experiment varied from 0.45% to 5.38%.
- Comparative analysis of various progressive failure models indicated that the use of high values of degradation parameters ($d_{f/m} = 1$) provided the best correlation with experimental results.
- Calculation of failure factors throughout the non-linear analysis with incremental load also indicated that the first failure occurrence is identified by the Huber-Mises-Hencky criterion applied to aluminum layers. This implies that the post-critical behavior of the 7-layered thin-walled GLARE columns is strongly controlled by aluminum plies.
- Based on stress state analysis in aluminum plies using Huber-Mises-Hencky criterion, compressive stress contributes mainly to aluminum plastic deformation.
- Stress state analysis in composite plies using Hashin failure criterion allowed recognizing that fiber rupture is mainly affected by shear stresses combined with shear strength in the plane parallel to the alignment of the fibers. Furthermore, the crushing effect of the matrix is predominantly caused by compressive stress and shear stress components.
- Based on the progressive failure analysis with various damage variables, subsequent propagation of matrix failure is primarily caused by cracking.
- Progressive failure assessment of top-hat members by FEM allowed estimating damage modes that were found to be in good agreement with experimental evidence.

Based on the literature survey, the abovementioned findings were confronted with other studies and discussed in the previous section. The presented approach in the context of damage analysis provided an efficient solution that can be applied with a good degree of success to assess the loading abilities and intra-laminar failure mechanism of thin-walled GLARE structures. Damage to the composite structure can also occur on the layer's boundary surface, causing inter-laminar delamination. Nevertheless, further detailed analysis of delamination requires an analysis of contact interface stresses and the growth of delamination using the bilinear cohesive contact model [68]. Delamination mechanisms of thin-walled GLARE members of channel sections subjected to axial compressive loading are investigated in the comprehensive study by Kamocka et al. [33]. Results shown in this study could also lead to a recommendation to select the damage variables that are applied in the failure analysis of thin-walled members subjected to compression. However, the authors suggest that different loading scenarios should be investigated in a comparable manner and supported by experiments to reduce discrepancies in the results.

CRediT authorship contribution statement

D. Banat: Conceptualization, Methodology, Software, Validation, Formal analysis, Investigation, Data curation, Writing – original draft, Writing – review & editing, Project administration, Funding acquisition. **R.J. Mania:** Conceptualization, Methodology, Validation, Writing – review & editing, Resources, Supervision. **R. Degenhardt:** Methodology, Validation, Writing – review & editing, Resources, Supervision.

Declaration of Competing Interest

The authors declare that they have no known competing financial interests or personal relationships that could have appeared to influence the work reported in this paper.

Acknowledgment

The first author has obtained funding as part of the financing of a doctoral scholarship from the National Science Center Poland, No. UMO-2019/32/T/ST8/00605.

Data availability

The raw/processed data required to reproduce these findings cannot be shared at this time as the data also forms part of an ongoing study.

References

[1] Moreira PMGP, da Silva LFM, de Castro PMST. Structural connections for lightweight metallic structures. 1st ed. Berlin: Springer Heidelberg; 2012. 10.1007/978-3-642-18187-0.
[2] Chróścielewski J, Miśkiewicz M, Pyrzowski Ł, Sobczyk B, Wilde K. A novel sandwich footbridge - Practical application of laminated composites in bridge design and in situ measurements of static response. Compos. B Eng. 2017;126: 153–61. https://doi.org/10.1016/J.COMPOSITESB.2017.06.009.
[3] Jones RM. Mechanics of Composite Materials. 2nd ed. Philadelphia: Taylor & Francis; 1999. 10.1007/BF00611782.
[4] Sinke J. Development of fibre metal laminates: Concurrent multi-scale modeling and testing. J. Mater. Sci. 2006;41:6777–88.
[5] Patil NA, Mulik SS, Wangikar KS, Kulkarni AP. Characterization of Glass Laminate Aluminium Reinforced Epoxy- A Review. Procedia Manuf. 2018;20:554–62. https://doi.org/10.1016/J.PROMFG.2018.02.083.
[6] Vlot A, Gunnink JW. Fibre Metal Laminates: An Introduction. Dordrecht: Springer Science & Business Media; 2001.
[7] Mania RJ, York CB. Buckling strength improvements for Fibre Metal Laminates using thin-ply tailoring. Compos. Struct. 2017;159:424–32. https://doi.org/10.1016/j.compstruct.2016.09.097.
[8] Khakimova R, Degenhardt R, Wilcken D. Experimental and numerical investigation of CFRP cylinders with circular cutouts under axial compression. Thin-Walled Struct. 2020;147. https://doi.org/10.1016/j.tws.2019.106526.
[9] Soltani P, Keikhosravy M, Oskouei RH, Soutis C. Studying the tensile behaviour of GLARE laminates: A finite element modelling approach. Appl. Compos. Mater. 2011;18:271–82. https://doi.org/10.1007/s10443-010-9155-x.
[10] Banat D, Kolakowski Z, Mania RJ. Investigations of fml profile buckling and post-buckling behaviour under axial compression. Thin-Walled Struct. 2016;107: 335–44. https://doi.org/10.1016/j.tws.2016.06.018.
[11] Wiedemann M, Sinapius M, editors. Adaptive, Tolerant and Efficient Composite Structures. Research Topics in Aerospace. 1st ed. Springer-Verlag Berlin Heidelberg; 2012. 10.1007/978-3-642-29190-6.
[12] Gliszczynski A, Kubiak T, Borkowski Ł. Experimental investigation of pre-damaged thin-walled channel section column subjected to compression. Compos. B Eng. 2018;147:56–68. https://doi.org/10.1016/j.compositesb.2018.04.022.
[13] Debski H, Teter A, Kubiak T, Samborski S. Local buckling, post-buckling and collapse of thin-walled channel section composite columns subjected to quasi-static compression. Compos. Struct. 2016;136:593–601. https://doi.org/10.1016/J.COMPSTRUCT.2015.11.008.
[14] Rozylo P, Debski H, Wysmulski P, Falkowicz K. Numerical and experimental failure analysis of thin-walled composite columns with a top-hat cross section under axial compression. Compos. Struct. 2018;204:207–16. https://doi.org/10.1016/j.compstruct.2018.07.068.
[15] Khakimova R, Castro SGP, Wilckens D, Rohwer K, Degenhardt R. Buckling of axially compressed CFRP cylinders with and without additional lateral load: Experimental and numerical investigation. Thin-Walled Structures 2017;119: 178–89. https://doi.org/10.1016/j.tws.2017.06.002.
[16] Debski H, Rozylo P, Gliszczynski A, Kubiak T. Thin-Walled Structures Numerical models for buckling, postbuckling and failure analysis of pre- damaged thin-walled composite struts subjected to uniform compression. Thin Walled Struct. 2019;139: 53–65. https://doi.org/10.1016/j.tws.2019.02.030.
[17] Al-Azzawi ASM, McCrory J, Kawashita LF, Featherston CA, Pullin R, Holford KM. Buckling and postbuckling behaviour of Glare laminates containing splices and doublers. Part 2: Numerical modelling. Compos. Struct. 2017;176:1170–87. https://doi.org/10.1016/j.compstruct.2017.04.030.
[18] Rozylo P, Falkowicz K. Stability and failure analysis of compressed thin-walled composite structures with central cut-out, using three advanced independent damage models. Compos. Struct. 2021;273:114298. https://doi.org/10.1016/J.COMPSTRUCT.2021.114298.
[19] Czapski P, Kubiak T. Selected problems of determining critical loads in sructures with stable post–critical behaviour. Mech. Mech. Eng. 2016;20:33–41.
[20] Debski H, Teter A, Kubiak T. Numerical and experimental studies of compressed composite columns with complex open cross-sections. Compos. Struct. 2014;118: 28–36. https://doi.org/10.1016/j.compstruct.2014.07.033.
[21] Kolakowski Z, Krolak M. Modal coupled instabilities of thin-walled composite plate and shell structures. Compos. Struct. 2006;76:303–13. https://doi.org/10.1016/j.compstruct.2005.02.022.
[22] Falkowicz K, Dębski H, Wysmulski P, Różyło P. The behaviour of compressed plate with a central cut-out, made of composite in an asymmetrical arrangement of layers. Compos. Struct. 2019;214:406–13. https://doi.org/10.1016/j.compstruct.2019.02.001.
[23] Wang D, Wen W. Three-dimensional progressive damage analysis of composite laminates containing a central hole subjected to compressive loading. Proceedings

of 2012 International Conference on Mechanical Engineering and Material Science, 2012, p. 367–71. 10.2991/mems.2012.19.
[24] Duarte APC, Díaz Sáez A, Silvestre N. Comparative study between XFEM and Hashin damage criterion applied to failure of composites. Thin-Walled Struct. 2017;115:277–88. https://doi.org/10.1016/j.tws.2017.02.020.
[25] Warren KC, Lopez-Anido RA, Vel SS, Bayraktar HH. Progressive failure analysis of three-dimensional woven carbon composites in single-bolt, double-shear bearing. Compos. B Eng. 2016;84:266–76. https://doi.org/10.1016/J.COMPOSITESB.2015.08.082.
[26] Czechowski L, Gliszczyński A, Bieniaś J, Jakubczak P, Majerski K. Failure of GFRP channel section beams subjected to bending - Numerical and experimental investigations. Compos. B Eng. 2017;111:112–23. https://doi.org/10.1016/j.compositesb.2016.11.057.
[27] Lin Y, Huang Y, Huang T, Liao B, Zhang D, Li C. Characterization of progressive damage behaviour and failure mechanisms of carbon fibre reinforced aluminium laminates under three-point bending. Thin-Walled Structures 2019;135:494–506. https://doi.org/10.1016/J.TWS.2018.12.002.
[28] Li W, Cai H, Li C, Wang K, Fang L. Progressive failure of laminated composites with a hole under compressive loading based on micro-mechanics. Adv. Compos. Mater 2014;23:477–90. https://doi.org/10.1080/09243046.2014.915105.
[29] Debski H, Rozylo P, Gliszczynski A, Kubiak T. Numerical models for buckling, postbuckling and failure analysis of pre-damaged thin-walled composite struts subjected to uniform compression. Thin-Walled Struct. 2019;139:53–65. https://doi.org/10.1016/j.tws.2019.02.030.
[30] Debski H, Rozylo P, Wysmulski P, Falkowicz K, Ferdynus M. Experimental study on the effect of eccentric compressive load on the stability and load-carrying capacity of thin-walled composite profiles. Compos. B Eng. 2021;226. https://doi.org/10.1016/j.compositesb.2021.109346.
[31] Abd-Elhady AA, Mubaraki MA, Sallam HE. Progressive failure prediction of pinned joint in quasi-isotropic laminates used in pipelines. Latin American J. Solids Struct. 2018;15. https://doi.org/10.1590/1679-78255061.
[32] Gliszczynski A, Kubiak T. Progressive failure analysis of thin-walled composite columns subjected to uniaxial compression. Compos. Struct. 2016;169:52–61.
[33] Kamocka M, Mania RJ. Post-buckling response of FML column with delamination. Compos. Struct. 2019;230:111511. https://doi.org/10.1016/J.COMPSTRUCT.2019.111511.
[34] Banat D, Mania RJ. Damage analysis of thin-walled GLARE members under axial compression – Numerical and experiment investigations. Compos. Struct. 2020;241:112102. https://doi.org/10.1016/j.compstruct.2020.112102.
[35] Lapczyk I, Hurtado JA. Progressive damage modeling in fiber-reinforced materials. Compos. A Appl. Sci. Manuf. 2007;38:2333–41. https://doi.org/10.1016/J.COMPOSITESA.2007.01.017.
[36] Liu PF, Zheng JY. Progressive failure analysis of carbon fiber/epoxy composite laminates using continuum damage mechanics. Mater. Sci. Eng. A 2008;485:711–7. https://doi.org/10.1016/J.MSEA.2008.02.023.
[37] Barbero EJ, Shahbazi M. Determination of material properties for ANSYS progressive damage analysis of laminated composites. Compos. Struct. 2017;176:768–79. https://doi.org/10.1016/j.compstruct.2017.05.074.
[38] Li N, Ju C. Mode-Independent and Mode-Interactive Failure Criteria for Unidirectional Composites Based on Strain Energy Density. Polymers 2020;12:1–18. https://doi.org/10.3390/POLYM12122813.
[39] Huang Y, Liu J, Huang X, Zhang J, Yue G. Delamination and fatigue crack growth behavior in Fiber Metal Laminates (Glare) under single overloads. Int. J. Fatigue 2015;78:53–60.
[40] Eyvazian A, Taghizadeh SA, Hamouda AM, Tarlochan F, Moeinifard M, Gobbi M. Buckling and crushing behavior of foam-core hybrid composite sandwich columns under quasi-static edgewise compression. J. Sandwich Struct. Mater. 2019. https://doi.org/10.1177/1099636219894665.
[41] Soden PD, Kaddour AS, Hinton MJ. Recommendations for designers and researchers resulting from the world-wide failure exercise. Compos. Sci. Technol. 2004;64:589–604.
[42] Kaddour AS, Hinton MJ, Smith PA, Li S. The background to the third world-wide failure exercise. J. Compos. Mater. 2013;47:2417–26. https://doi.org/10.1177/0021998313499475.
[43] dos Santos DG, Carbas RJC, Marques EAS, da Silva LFM. Reinforcement of CFRP joints with fibre metal laminates and additional adhesive layers. Compos. B Eng. 2019;165:386–96. https://doi.org/10.1016/J.COMPOSITESB.2019.01.096.
[44] Seyed Yaghoubi A, Liu Y, Liaw B. Low-Velocity Impact on GLARE 5 Fiber-Metal Laminates: Influences of Specimen Thickness and Impactor Mass. J. Aerosp. Eng. 2012;25:409–20. https://doi.org/10.1061/(ASCE)AS.1943-5525.0000134.
[45] Rodi R, Alderliesten R, Benedictus R. An Experimental Approach to Investigate Detailed Failure Mechanisms in Fibre Metal Laminates BT - ICAF 2009, Bridging the Gap between Theory and Operational Practice. In: Bos MJ, editor., Dordrecht: Springer Netherlands; 2009, p. 493–512.
[46] Kamocka M, Zglinicki M, Mania RJ. Multi-method approach for FML mechanical properties prediction. Compos. B Eng. 2016;91:135–43. https://doi.org/10.1016/j.compositesb.2016.01.014.
[47] Bieniaś J. Fibre Metal Laminates - some aspects of manufacturing process, structure and selected properties. Composites Theory Pract. 2011;11:39–43.
[48] Barbero EJ. Finite Element Analysis of Composite Materials. 2nd ed. Boca Raton: CRC Press; 2007.
[49] Wang H, Chen L, Ye F, Wang J. A multi-hierarchical successive optimization method for reduction of spring-back in autoclave forming. Compos. Struct. 2018;188:143–58. https://doi.org/10.1016/J.COMPSTRUCT.2018.01.010.
[50] Bieniaś J, Mania RJ, Jakubczak P, Majerski K. The issues of manufacturing of geometrically complicated elements by using FML laminates. Compos. Theory Pract. 2015;15:243–9.
[51] Megson THG. An introduction to aircraft structural analysis. 1st ed. Oxford: Butterworth-Heinemann; 2010.
[52] Prasad NE, Wanhill RJH, editors. Aerospace materials and material technologies. 1st ed. Singapore: Springer; 2017. 10.1007/978-981-10-2134-3.
[53] Banat D, Mania RJ. Stability and strength analysis of thin-walled GLARE composite profiles subjected to axial loading. Compos. Struct. 2019;212:338–45. https://doi.org/10.1016/j.compstruct.2019.01.052.
[54] Ansys 18.2. User's Guide ANSYS® Academic Research, Help System n.d.
[55] Barbero EJ, Cosso FA, Roman R, Weadon TL. Determination of material parameters for Abaqus progressive damage analysis of E-glass epoxy laminates. Compos. B Eng. 2013;46:211–20. https://doi.org/10.1016/j.compositesb.2012.09.069.
[56] Rafiee R, Torabi MA, Maleki S. Investigating structural failure of a filament-wound composite tube subjected to internal pressure: Experimental and theoretical evaluation. Polym. Test. 2018;67:322–30. https://doi.org/10.1016/J.POLYMERTESTING.2018.03.020.
[57] Rafiee R, Torabi MA. Stochastic prediction of burst pressure in composite pressure vessels. Compos. Struct. 2018;185:573–83. https://doi.org/10.1016/J.COMPSTRUCT.2017.11.068.
[58] Banat D, Mania RJ. Progressive failure analysis of thin-walled Fibre Metal Laminate columns subjected to axial compression. Thin-Walled Struct. 2018;122:52–63. https://doi.org/10.1016/j.tws.2017.09.034.
[59] Rafiee R, Habibagahi MR. Evaluating mechanical performance of GFRP pipes subjected to transverse loading. Thin-Walled Struct. 2018;131:347–59. https://doi.org/10.1016/J.TWS.2018.06.037.
[60] Rafiee R, Abbasi F. Numerical and Experimental Analyses of the Hoop Tensile Strength of Filament-Wound Composite Tubes. Mechanics of Composite Materials 2020 56:4 2020;56:423–36. 10.1007/S11029-020-09894-2.
[61] Maimí P, Camanho PP, Mayugo JA, Dávila CG. A continuum damage model for composite laminates: Part I - Constitutive model. Mech. Mater. 2007;39:897–908. https://doi.org/10.1016/j.mechmat.2007.03.005.
[62] Subramanyam N, Vijayakumar R, Rao KP. Prediction Of Progressive Damage And Failure Analysis Of Rotorcraft Composite Nose Cowling By Continuum Damage Mechanics Model. Mater. Today. Proc. 2018;5:4335–44. https://doi.org/10.1016/j.matpr.2017.11.699.
[63] Donadon MV, Iannucci L, Falzon BG, Hodgkinson JM, de Almeida SFM. A progressive failure model for composite laminates subjected to low velocity impact damage. Comput. Struct. 2008;86:1232–52. https://doi.org/10.1016/J.COMPSTRUC.2007.11.004.
[64] Tonatto MLP, Forte MMC, Tita V, Amico SC. Progressive damage modeling of spiral and ring composite structures for offloading hoses. Mater. Des. 2016;108:374–82. https://doi.org/10.1016/j.matdes.2016.06.124.
[65] Barbero EJ, Abdelal GF, Caceres A. A micromechanics approach for damage modeling of polymer matrix composites. Compos. Struct. 2005;67:427–36. https://doi.org/10.1016/j.compstruct.2004.02.001.
[66] Banat D, Mania RJRJ. Comparison of failure criteria application for FML column buckling strength analysis. Compos. Struct. 2016;140:806–15. https://doi.org/10.1016/j.compstruct.2016.01.024.
[67] Remmers JJC, De Borst R. Delamination buckling of fibre–metal laminates. Compos. Sci. Technol. 2001;61:2207–13. https://doi.org/10.1016/S0266-3538(01)00114-2.
[68] Heimbs S, Heller S, Middendorf P, Hähnel F, Weiße J. Low velocity impact on CFRP plates with compressive preload: Test and modelling. Int. J. Impact Eng. 2009;36:1182–93. https://doi.org/10.1016/J.IJIMPENG.2009.04.006.